



Probing the Jet–Torus Interaction in the Radio Galaxy NGC 1052 by Sulfur-bearing Molecules

Seiji Kamenno^{1,2}, Satoko Sawada-Satoh³, C. M. Violette Impellizzeri⁴, Kotaro Kohno^{5,6}, Sergio Martín^{1,7}, Daniel Espada^{8,9}, Naomasa Nakai¹⁰, Hajime Sugai¹¹, Yuichi Terashima¹², Minju M. Lee^{13,14}, and Nozomu Kawakatu¹⁵

¹ Joint ALMA Observatory, Alonso de Córdova 3107 Vitacura, Santiago 763-0355, Chile; seiji.kamenno@alma.cl

² National Astronomical Observatory of Japan, 2-21-1 Osawa, Mitaka, Tokyo 181-8588, Japan

³ Graduate School of Science, Osaka Metropolitan University, 1-1 Gakuen-cho, Naka-ku, Sakai, Osaka 599-8531, Japan

⁴ Leiden Observatory, Leiden University, PO Box 9513, 2300 RA, Leiden, The Netherlands

⁵ Institute of Astronomy, Graduate School of Science, The University of Tokyo, 2-21-1 Osawa, Mitaka, Tokyo 181-0015, Japan

⁶ Research Center for the Early Universe, Graduate School of Science, The University of Tokyo, 7-3-1 Hongo, Bunkyo-ku, Tokyo 113-0033, Japan

⁷ European Southern Observatory, Alonso de Córdova 3107 Vitacura, Santiago 763-0355, Chile

⁸ Departamento de Física Teórica y del Cosmos, Campus de Fuentenueva, Universidad de Granada, E-18071 Granada, Spain

⁹ Instituto Carlos I de Física Teórica y Computacional, Facultad de Ciencias, E-18071, Granada, Spain

¹⁰ School of Science, Kwansei Gakuin University, 1 Gakuen Uegahara, Sanda, Hyogo 669-1330, Japan

¹¹ Environment and Energy Department, Japan Weather Association, Sunshine 60 Bldg. 55F, 3-1-1 Higashi-Ikebukuro, Toshima-ku, Tokyo 170-6055, Japan

¹² Graduate School of Science and Engineering, Ehime University, 2-5 Bunkyo-cho, Matsuyama, Ehime 790-8577, Japan

¹³ Cosmic Dawn Center (DAWN), Jagtvej 128, DK-2200 Copenhagen N, Denmark

¹⁴ DTU-Space, Technical University of Denmark, Elektrovej 327, DK-2800 Kgs. Lyngby, Denmark

¹⁵ Faculty of Natural Sciences, National Institute of Technology, Kure College, 2-2-11 Agaminami, Kure, Hiroshima 737-8506, Japan

Received 2022 December 2; revised 2023 January 10; accepted 2023 January 17; published 2023 February 21

Abstract

The radio galaxy NGC 1052 casts absorption features of sulfur-bearing molecules, H₂S, SO, SO₂, and CS toward the radio continuum emission from the core and jets. Using the Atacama Large Millimeter/submillimeter Array, we have measured the equivalent widths of SO absorption features in multiple transitions and determined the temperatures of 344 ± 43 K and 26 ± 4 K in submillimeter and millimeter wavelengths, respectively. Since submillimeter and millimeter continuum represents the core and jets, the high and low temperatures of the absorbers imply a warm environment in the molecular torus and cooler downstream flows. The high temperature in the torus is consistent with the presence of 22 GHz H₂O maser emission, vibrationally excited HCN and HCO⁺ absorption lines, and sulfur-bearing molecules in the gas phase released from dust. The origin of the sulfur-bearing gas is ascribed to the evaporation of the icy dust component through a jet–torus interaction. Shock heating is the sole plausible mechanism to maintain such a high temperature of gas and dust in the torus. The implication of the jet–torus interaction also supports the collimation of the sub-relativistic jets by the gas pressure of the torus.

Unified Astronomy Thesaurus concepts: Active galactic nuclei (16); Molecular spectroscopy (2095); Radio galaxies (1343); Radio jets (1347)

1. Introduction

A dusty molecular torus in active galactic nuclei (AGNs) resides in the central parsec scale (García-Burillo et al. 2016; Gallimore et al. 2016; Impellizzeri et al. 2019) and is recognized as a key component that plays significant roles in mass accretion onto the central engine, collimation of jets, and diversity of appearance depending on viewing angles (Antonucci 1993). Observational studies of AGN tori are essential to understand the nature of AGNs, mass accretion processes, and jet collimation mechanisms.

The radio galaxy NGC 1052 is a unique target to probe an AGN torus that is seen nearly edge-on while hiding the nucleus (Kamenno et al. 2020). The torus harbors H₂O masers (Braatz et al. 1994, 2003; Claussen et al. 1998; Kamenno et al. 2005) that allows sub-parsec-scale kinetic studies of molecular gas with very long baseline interferometry (VLBI) resolution (Sawada-Satoh et al. 2008). The presence of a 22 GHz H₂O maser requires excitation under hot (~ 400 K) and dense ($\sim 10^7$

cm^{−3}) conditions of the molecular gas (Elitzur et al. 1989). The torus casts various absorption features of plasma free–free absorption (Kamenno et al. 2001, 2003; Kadler et al. 2004), dust obscuration and scattering (Barth et al. 1999), photoelectric absorption (Baloković et al. 2021), H I (Vermeulen et al. 2003), and the molecules of OH, HCO⁺, HCN, CO, SO, SO₂, CS, CN, and H₂O (Omar et al. 2002; Liszt & Lucas 2004; Impellizzeri et al. 2008; Sawada-Satoh et al. 2016, 2019; Kamenno et al. 2020). The presence of vibrationally excited HCN and HCO⁺ absorption (Kamenno et al. 2020) implies pumping by infrared radiation from warm dust (Lahuis et al. 2007).

NGC 1052 is known to have two-sided jets with a sub-relativistic bulk speed of $0.26c$ – $0.53c$ (Vermeulen et al. 2003). Multifrequency VLBI observations have revealed the core and double-sided jet structure of NGC 1052. The core shows a peaked flat spectrum at frequencies higher than 43 GHz (Baczko et al. 2016; Sawada-Satoh et al. 2016, 2019), while it is optically thick at lower frequencies due to free–free absorption hidden in a gap (Kellermann et al. 1999; Kamenno et al. 2001, 2003; Vermeulen et al. 2003; Kadler et al. 2004). The jets show a steep spectrum implying optically thin synchrotron emission. The brightness of the jets decreases as they flow downstream (Kamenno et al. 2001, 2003;



Original content from this work may be used under the terms of the [Creative Commons Attribution 4.0 licence](https://creativecommons.org/licenses/by/4.0/). Any further distribution of this work must maintain attribution to the author(s) and the title of the work, journal citation and DOI.

Vermeulen et al. 2003; Kadler et al. 2004; Baczkó et al. 2016, 2019). The jet is collimated in a cylindrical shape with a width of $1.3 \times 10^3 R_S$ (Schwarzschild radii) inside the break point of $10^4 R_S$ from the core, and transit to a conical structure outside the break point (Nakahara et al. 2020). Baczkó et al. (2022) found a more complex upstream structure, with neither a cylindrical nor a parabolic shape, with the second break point at $3 \times 10^3 R_S$. These studies on the jet width imply collimation by surrounding dense material such as the molecular torus.

If the torus is confining the jet width by external gas pressure, we expect an interaction between sub-relativistic jets and torus gas, and shocks generated by the interaction. Fromm et al. (2019) modeled overpressured jets in a decreasing pressure ambient medium for NGC 1052 and simulated VLBI images reproducing the core-jet structure at 43 GHz and the gap at 22 GHz. The model indicates that pressure mismatch between the jet and the ambient medium forms a recollimation shock at the nozzle pinching the jet boundary. Observational follow-up is needed to probe such a jet–torus interaction.

Sulfur-bearing molecules are known to be good shock tracers in interstellar clouds (Pineau des Forets 1993), young stellar objects (Bachiller & Perez Gutierrez 1997), protoplanetary disks (Nomura et al. 2020), evolved stars (Adegoke et al. 2013), starburst galaxies (Martin et al. 2003; Martín et al. 2005; Minh et al. 2007), and ultraluminous infrared galaxies (Sato et al. 2022). Observations of H_2S , SO, SO_2 , and CS in the molecular torus of NGC 1052 would provide clues about jet–torus interaction.

In this article, we report investigations of sulfur-bearing molecular absorption lines toward the radio continuum of NGC 1052. Our primary aim is to measure the temperature of the gas by comparing line equivalent widths (EWs) at various excitation levels. Then, we examine the jet–torus interaction as a heat source of the gas and dust in the torus.

We employ the systemic velocity of $V_{LSR,radio} = 1492 \text{ km s}^{-1}$ or $V_{hel} = 1505 \text{ km s}^{-1}$ (Kameno et al. 2020), the bolometric luminosity of $L_{bol} = 10^{42.3} \text{ erg s}^{-1} = 2 \times 10^{35} \text{ W}$ (Guo et al. 2014), and the black hole mass of $M_{BH} = 1.5 \times 10^8 M_\odot$ (Woo & Urry 2002). The Schwarzschild radius is $R_s = 3 \text{ au}$, corresponding to $0.17 \mu\text{arcsec}$. Data reduction scripts are available in the GitHub repository¹⁶ together with spectral data.

2. Observations and Results

We have carried out Atacama Large Millimeter/submillimeter Array (ALMA) Band 3 (85.0–88.8 GHz and 97.0–100.4 GHz) and Band 4 (126.4–130.1 GHz and 138.3–141.7 GHz) observations of NGC 1052 targeting SO, CS, SiO, and HCN molecules. The Band 3 frequency is set to cover the transitions $SO J_N = 2_2-1_1$ (permitted), HCN $J = 1-0$ and SiO $J = 2-1$, $v = 0$ and $v = 1$ in the upper sideband (USB), and CS ($J = 2-1$), $SO J_N = 3_2-3_1$ (permitted), and 4_5-4_4 (forbidden) in the lower sideband (LSB). The Band 4 USB covers $SO J_N = 3_3-2_2$ (permitted), SiO $J = 3-2$, and $v = 0, 1, 2$, while the LSB covers the forbidden SO transitions. Some SO_2 transitions reside in the frequency coverage.

J0238+1636 and J0243-0550 were used as the bandpass and phase calibrators, respectively, in both bands. We also used NGC 1052 for self-calibration. Table 1 lists the observation log.

The continuum images at both bands consist of an unresolved point-like component with 1.127 and 0.859 Jy at 92.7 and 134.1 GHz, respectively, as shown in the insets of Figures 1 and 2. No significant extended structure is identified with the image rms of 37 and $25 \mu\text{Jy beam}^{-1}$, respectively.

We took spectra in a single pixel at the center of the point-like component as shown in Figures 1 and 2. The four plots represent the LSB and USB in Bands 3 and 4, respectively. Spectra of the phase calibrator, J0243-0550, are presented in cyan as the control. Line species are marked by red vertical ticks. Velocity scales with respect to the systemic velocity $\pm 400 \text{ km s}^{-1}$ are also tagged on a line feature in each plot. The identified features are listed in Table 2.

HCN $J = 1-0$ is the most prominent feature, which shows an asymmetric profile with a sharp edge on the redshifted side. $H^{13}\text{CN } J = 1-0$ absorption is also detected with a more serrated profile than that of the $H^{12}\text{CN}$ feature. The $\text{HCO}^+ J = 1-0$ feature is partially covered by our spectral setting. The ratio of the HCN-to- HCO^+ peak opacity is 2.1 ± 0.2 , being consistent with the Korean VLBI Network (KVN) results (Sawada-Satoh et al. 2019).

All permitted SO absorption features, $J_N = 2_2-1_1$, 3_2-2_1 , and 3_3-2_2 are clearly detected. $SO J_N = 4_5-4_4$ is the sole forbidden line and is clearly detected. The 8_8-7_8 feature is marginal and higher- J forbidden lines are not detected.

We have also identified SO_2 absorption features of $J_{Ka,Kc} = 10_{2,8}-10_{1,9}$ and $12_{2,10}-12_{1,11}$. The feature of the $12_{2,10}-12_{1,11}$ transition overlaps with $SO J_N = 3_3-2_2$. The $6_{2,4}-6_{1,5}$ feature is not significantly detected. CS $J = 2-1$ absorption feature is marginally detected with a significance of 3.6 times the rms level. No significant SiO absorption was detected. Possible SiO $J = 2-1$, $v = 1$ emission with $4.4 \pm 0.26 \text{ mJy}$ appeared at 56.7 km s^{-1} . We do not argue for this feature before confirmation in another transition.

Figure 3 shows optical depth profiles of the HCN and SO absorption lines to be compared with higher frequency transitions acquired in the ALMA Band 6 and Band 7 observations reported in Kameno et al. (2020). While absorption profiles in Bands 6 and 7 consist of a single component peaked at the systemic velocity with wider redward tails, those in Bands 3 and 4 consist of multiple components with the redshifted peaks at $164 \pm 6 \text{ km s}^{-1}$ and sharp redward edges around 210 km s^{-1} , and shallow blueward slopes down to -190 km s^{-1} . The velocity ranges of Bands 3 and 4 absorption features are settled within the HCN $J = 4-3$ velocity range of $V_{sys}^{+382}_{-318} \text{ km s}^{-1}$.

We have measured $EW = \int \tau(v) dv$ by integrating the optical depth profile in the velocity range of $(-222, 258) \text{ km s}^{-1}$ after subtracting the line-free baseline in $(-312, -222)-(258, 478) \text{ km s}^{-1}$. The standard error in the EW is dominated by uncertainty in the baseline-level determination. For $SO J_N = 3_3-2_2$, we corrected the contamination of $SO_2 12_{2,10}-12_{1,11}$ by assuming that the extra EW equals the mean of those in $10_{2,8}-10_{1,9}$ and $12_{2,10}-12_{1,11}$. We derived total column density, N_{tot} , for SO, HCN, HCO^+ , and CS assuming local thermodynamic equilibrium as

$$N_{tot} = \frac{3kT_{ex}}{8\pi^3\mu^2B(2J+1)} \exp\left(\frac{hB}{3kT_{ex}}\right) \times \exp\left(\frac{hBJ(J+1)}{kT_{ex}}\right) \left[\exp\left(\frac{h\nu}{kT_{ex}}\right) - 1 \right]^{-1} EW, \quad (1)$$

¹⁶ <https://github.com/kamenoseiji/ALMA-2016.1.00375.S>

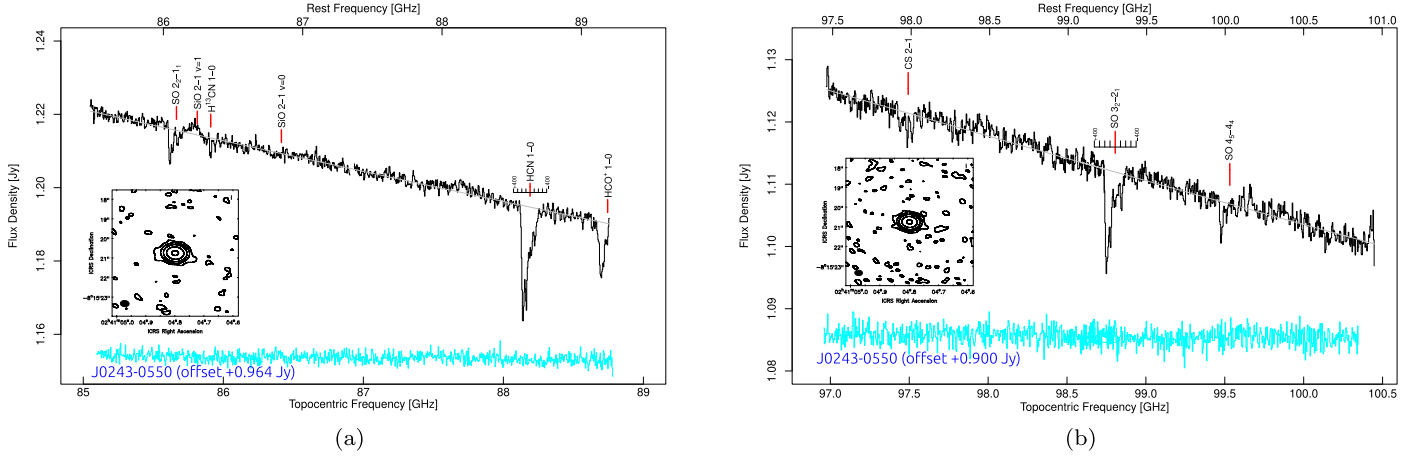


Figure 1. Spectra in the single pixel at the center of NGC 1052 in Band 3. (a) LSB (85.0–88.8 GHz). (b) USB (97.0–100.4 GHz). Top and bottom abscissas stand for the frequency at the source frame and topocentric frame, respectively. Red vertical markers indicate line species at the systemic velocity. Spectra of J0243-0550, offset by 0.964 and 0.900 Jy, are shown in cyan. Continuum maps are shown in the inset with the contour levels of $75 \mu\text{Jy beam}^{-1} \times \text{powers of } 10$.

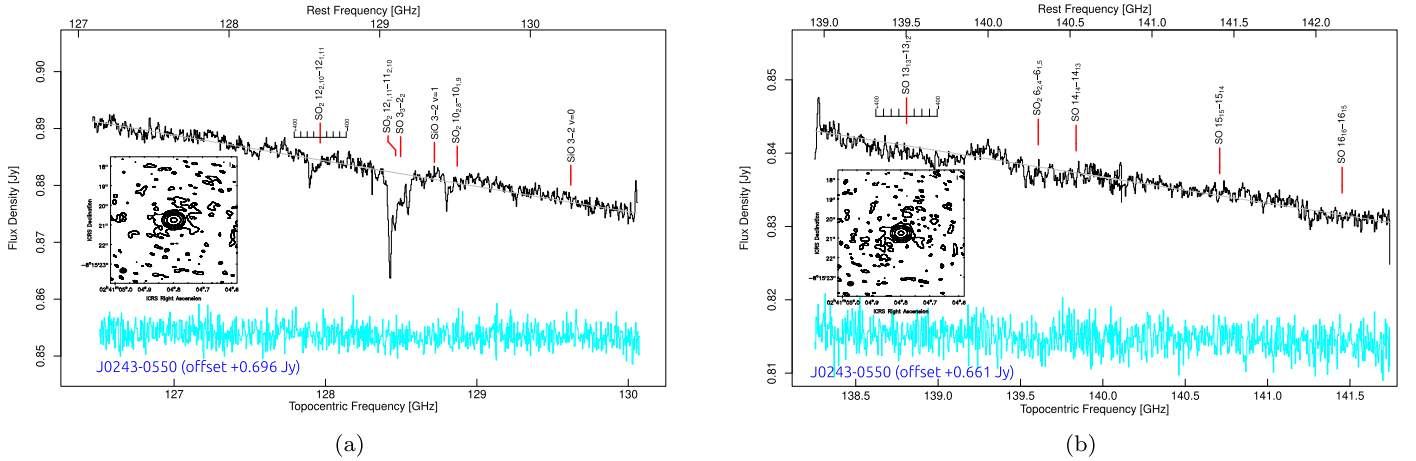


Figure 2. Spectra of NGC 1052 in Band 4. (a) LSB (126.4–130.1 GHz). (b) USB (138.3–141.7 GHz). Spectra of J0243-0550, offset by 0.696 and 0.661 Jy, are shown in cyan. Continuum maps are shown in the inset with the contour levels of $50 \mu\text{Jy beam}^{-1} \times \text{powers of } 10$.

Table 1
Observation Log

Date	ExecBlock UID uid://A002/	ν_{obs} GHz	N_{ant}	Beam Size and P.A.	Spectral Resolution MHz, km s^{-1}	Image rms mJy beam^{-1}
(1)	(2)	(3)	(4)	(5)	(6)	(7)
2017-7-28	Xc2bb44/X1baf	92.7	45	$0''.42 \times 0''.30$, $+86^\circ$	3.9, 12	0.26
2017-7-23	Xc27dd7/X2e85	134.1	46	$0''.34 \times 0''.25$, -87°	3.9, 9	0.20

Note. (1) Year-month-day; (3) center frequency; (4) number of antennas; (5) synthesized beam size (FWHM in major and minor axes) and position angle (P.A.); (6) spectral resolution in megahertz and velocity resolution in kilometers per second; (7) image rms of channel maps.

where k is the Boltzmann constant, h is the Planck constant, μ is the permanent dipole moment of the molecule, B is the rotational constant, and ν is the rest frequency. We applied the excitation temperature, $T_{\text{ex}} = 26$ K, obtained in Section 3.2. The EW and N_{tot} values are listed in Table 2.

3. Discussion

Four species of sulfur-bearing molecules, H_2S , SO, SO_2 , and CS, have been detected in absorption toward the nucleus of

NGC 1052. We discuss the origin of these molecules, the physical conditions, and the heating mechanism.

3.1. Line Profiles

It is remarkable that optical depth profiles are classified into two distinct groups: (1) multicomponent asymmetric profile peaked at a redshifted velocity of $164 \pm 6 \text{ km s}^{-1}$, presented in Figure 3(a), and (2) a single component peaked at the systemic velocity with wider redward tails, shown in Figure 3(b). The

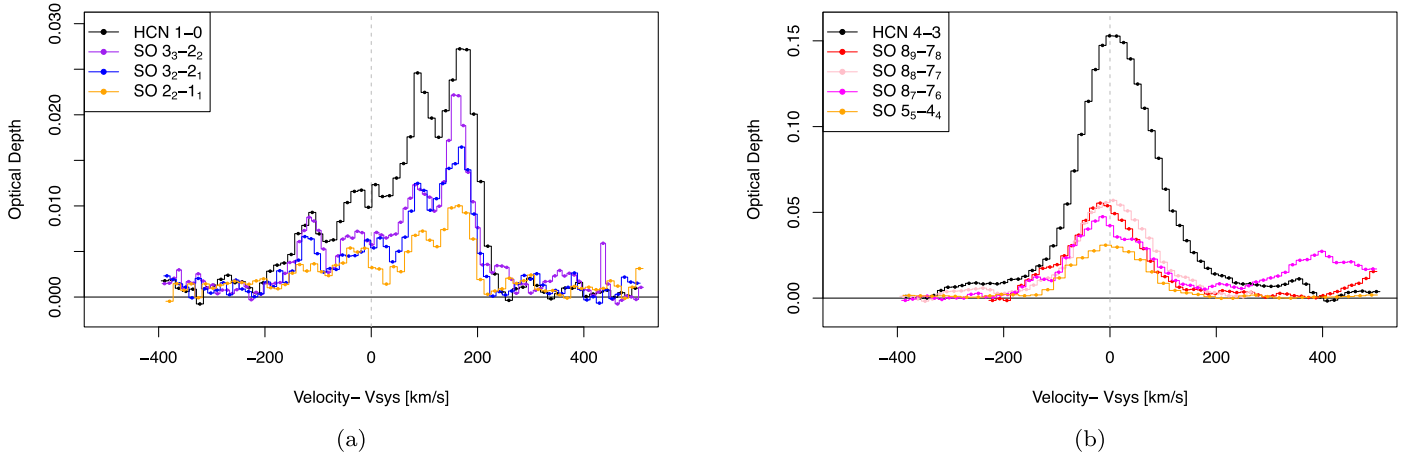


Figure 3. (a) Optical depth profiles acquired in ALMA Band 3 and Band 4 observations. Black, purple, blue, and orange lines stand for the HCN $J = 1-0$, SO $J_N = 3_3-2_2$, SO $J_N = 3_2-2_1$, and SO $J_N = 2_2-1_1$ transitions, respectively. (b) Optical depth profiles of HCN and SO transitions in ALMA Band 6 and Band 7 observations presented in Kameno et al. (2020). The dashed vertical lines represent the systemic velocity.

Table 2
Identified Absorption Lines

Species	Transition	ν_{rest} (GHz)	τ_{max}	Velocity (km s $^{-1}$)	EW (km s $^{-1}$)	N_{tot} (10^{14} cm $^{-2}$)
(1)	(2)	(3)	(4)	(5)	(6)	(7)
SO	$J_N = 2_2-1_1$	86.09395	0.0079 ± 0.0006	165	1.28 ± 0.07	2.33 ± 0.13
	$J_N = 3_2-2_1$	99.29987	0.0151 ± 0.0009	170	2.33 ± 0.11	2.55 ± 0.12
	$J_N = 3_3-2_2$	129.13892	0.0214 ± 0.0012	155	3.02 ± 0.11	2.47 ± 0.09
	$J_N = 4_5-4_4$	100.02964	0.0061 ± 0.0012	167	0.72 ± 0.11	...
	$J_N = 8_8-7_8$	129.95366	0.0027 ± 0.0008	105	0.23 ± 0.07	...
	$J_N = 13_{13}-13_{12}$	139.50251	0.0030 ± 0.0009	229	<0.075	...
	$J_N = 14_{14}-14_{13}$	140.53709	0.0033 ± 0.0011	408	0.15 ± 0.05	...
	$J_N = 15_{15}-15_{14}$	141.41311	0.0013 ± 0.0009	482	0.14 ± 0.06	...
	$J_N = 16_{16}-16_{15}$	142.16005	0.0032 ± 0.0011	408	<0.09	...
SO $_2$	$J_{Ka,Kc} = 6_{2,4}-6_{1,5}$	140.30617	0.0037 ± 0.0011	159	<0.07	...
	$J_{Ka,Kc} = 10_{2,8}-10_{1,9}$	129.51481	0.0060 ± 0.0008	161	0.60 ± 0.07	...
	$J_{Ka,Kc} = 12_{1,11}-11_{2,10}$	129.10583
	$J_{Ka,Kc} = 12_{2,10}-12_{1,11}$	128.60513	0.0059 ± 0.0008	164	0.65 ± 0.07	...
HCN	$J = 1-0$	88.63185	0.0266 ± 0.0007	166	4.95 ± 0.07	3.15 ± 0.45
H 13 CN	$J = 1-0$	86.33992	0.0045 ± 0.0013	-4	0.64 ± 0.10	0.43 ± 0.07
HCO $^+$	$J = 1-0$	89.18853	0.0128 ± 0.0013	149	1.83 ± 0.10	0.68 ± 0.05
CS	$J = 2-1$	97.98095	0.0050 ± 0.0011	17	0.47 ± 0.13	0.41 ± 0.11

Note. (1) Line species; (2) transition; (3) rest frequency; (4) peak optical depth; (5) peak velocity with respect to the systemic velocity; (6) $\text{EW} = \int \tau dV$. The optical depth of SO $_2$ $J_{Ka,Kc} = 12_{1,11}-11_{1,10}$ cannot be measured and it contaminates that of SO $J_N = 3_3-2_2$; (7) total column density assuming $T_{\text{ex}} = 26$ K.

two groups are discriminated by frequencies below 129 GHz and above 214 GHz. Hereafter, we refer to the two groups as *millimeter absorption* and *submillimeter absorption*.

We averaged the optical depths for each group to highlight the difference and plotted them in Figure 4. The average of submillimeter and millimeter optical depths consist of the line species plotted in Figure 3; submillimeter: HCN $J = 4-3$, SO $J_N = 8_9-7_8$, 8_8-7_7 , 8_7-7_6 , and 5_5-4_4 , and millimeter: HCN $J = 1-0$, SO $J_N = 3_3-2_2$, 3_2-2_1 , and 2_2-1_1 . While the submillimeter optical depth can be fitted by a single Gaussian component, millimeter absorption requires at least five components. The parameters of the Gaussian components are listed in Table 3. These components are also presented in Figure 4. The velocities of the submillimeter and millimeter components shown by the green-dashed line coincide with the systemic velocity. The millimeter absorption additionally contains two stronger redshifted and two weaker blueshifted components. These redshifted and blueshifted components

show significantly narrower velocity widths than that of the systemic velocity component.

3.2. Temperature of the Absorber

We attempt to measure rotation temperature, T_{rot} , by comparing the EWs of SO in multiple transitions as

$$\frac{\text{EW}}{2N_l + 1} \sim n_0 \exp\left(-\frac{E_k}{T_{\text{rot}}}\right),$$

for these millimeter and submillimeter absorbers separately. Here N_l and E_k are the lower-level rotational angular momentum and energy, respectively, and n_0 stands for the intercept. The best fit resulted in $T_{\text{rot}} = 26 \pm 4$ and 344 ± 43 K for the millimeter and submillimeter absorbers, respectively. Figure 5 shows a Boltzmann diagram of the detected permitted SO absorption lines. The SO $J_N = 3_3-2_2$, 3_2-2_1 , and 2_2-1_1

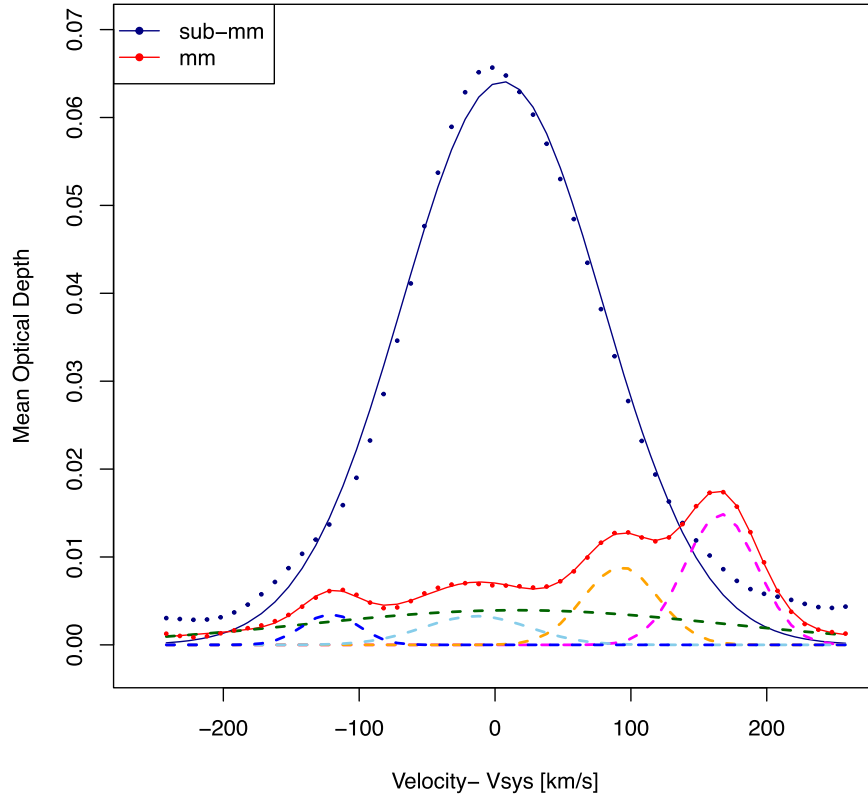


Figure 4. Average optical depths in submillimeter and millimeter absorption. Filled circles in navy blue and red denote the average optical depths in submillimeter (HCN $J = 4-3$, SO $J_N = 8_9-7_8$, 8_8-7_7 , 8_7-7_6 , and 5_5-4_4) and millimeter (HCN $J = 1-0$, SO $J_N = 3_3 = 2_2$, 3_2-2_1 , and 2_2-1_1) absorption, respectively. Solid lines in navy blue and red indicate the Gaussian fitting for the average optical depth in submillimeter (single component) and millimeter (five components) absorption, respectively. Gaussian components of the millimeter absorption are shown by dashed lines in magenta, orange, green, cyan, and blue. The parameters of the Gaussian components are listed in Table 3.

Table 3
Parameters of the Gaussian Absorber Components

Component	Peak Opacity	Velocity km s ⁻¹	FWHM km s ⁻¹
(1)	(2)	(3)	(4)
Submillimeter (navy blue)	0.0642 ± 0.0009	5.5 ± 1.1	174.3 ± 2.7
Millimeter (magenta)	0.0149 ± 0.0004	166.1 ± 0.6	62.8 ± 1.5
Millimeter (orange)	0.0089 ± 0.0008	92.5 ± 0.9	64.9 ± 2.9
Millimeter (green)	0.0039 ± 0.0012	16.1 ± 5.8	360.0 ± 49
Millimeter (cyan)	0.0033 ± 0.0011	-13.7 ± 2.4	92.1 ± 17
Millimeter (blue)	0.0035 ± 0.0004	-121.0 ± 1.0	48.6 ± 4.0

Note. (1) Components with the colors denoted in Figure 4; (2) peak optical depth; (3) peak velocity with respect to the systemic velocity; (4) velocity width at FWHM.

transitions below 129 GHz are plotted in red markers. We added the 5_5-4_4 , 8_7-7_6 , 8_8-7_7 , and 8_9-7_8 transitions above 214 GHz in blue markers using data from Kameno et al. (2020). To correct for HC¹⁵N contamination into an 8_8-7_7 feature, we applied a proportional allocation of $\text{EW}(\text{SO})/\text{EW}(\text{HC}^{15}\text{N}) = 7.9:1.2$ using the result of two-component Gaussian decomposition.

The high temperature in the submillimeter regime is consistent with the presence of vibrationally excited ($v_2 = 1$) HCN and HCO⁺ lines (Kameno et al. 2020). The presence of SO₂ absorption features also supports the warm environment because SO₂ would freeze onto dust particles under $T < 130$ K

(Nomura et al. 2020). Kameno et al. (2020) discussed the physical properties of the molecular torus, for the cases of $T = 50, 100, 230$, and 500 K, to explain the obtained absorption-line features. Our results rule out the 50 and 100 K cases, and are consistent with 230 and 500 K, which yields the covering factor of $f_{\text{cov}} = 0.17^{+0.06}_{-0.03}$, the geometrical thickness of $\Theta = 0.4-1.0$, and the radius of $R = 2.4 \pm 1.3$ pc. Non-detection of SiO features indicates that the temperature must be below the sublimation temperature of silicates.

The temperature of the millimeter absorber is below the freeze-out temperatures of H₂, SO, and SO₂. This indicates that sulfur-bearing molecules have been cooled after being released from warm dust. We discuss the origin of the cool millimeter absorber in Sections 3.3 and 3.4.

3.3. Location of Absorbers

Because an absorber must locate in front of the background continuum source along the line of sight, a frequency-dependent continuum structure can cause a difference in the absorption profiles. While the continuum source is spatially unresolved in ALMA observations with the synthesized beam of $\sim 0''.3$, multifrequency VLBI studies have revealed sub-parsec-scale structures composed of core and double-sided jets. The core is optically thick and hidden in the gap below 43 GHz due to free-free absorption (Kellermann et al. 1999; Kameno et al. 2001, 2003; Vermeulen et al. 2003; Kadler et al. 2004), and appears at higher frequencies with a peaked flat spectrum (Baczko et al. 2016; Sawada-Satoh et al. 2016, 2019). On the other hand, the jets have a steep spectrum with a brightness

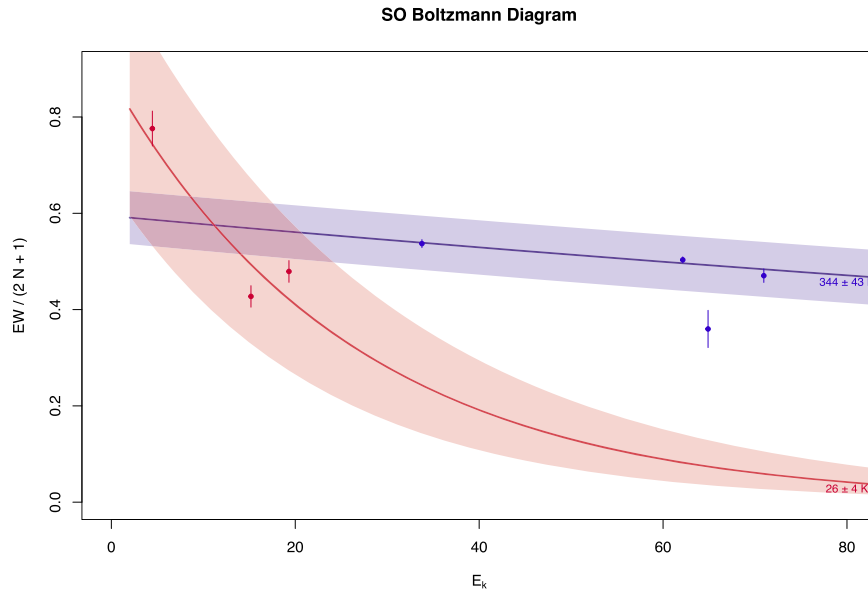


Figure 5. Boltzmann diagram of the SO absorption feature. Red and blue lines indicate the best fits for millimeter and submillimeter SO absorptions, respectively. The transparent bands show the uncertainties of the temperatures and intercepts.

gradient inward of the core (Kameno et al. 2001, 2003; Vermeulen et al. 2003; Kadler et al. 2004; Bacsko et al. 2016, 2019) with a peak in gigahertz frequencies (Fromm et al. 2019). As a result, the extension of the jet becomes longer at a lower frequency. The footpoints of the jets are optically thick below 22 GHz with a gap due to the free-free absorption. Although no VLBI image at the submillimeter wavelength has been published to date, the submillimeter continuum emission is putatively dominated by the core component rather than the jet. Figure 6 shows a possible decomposition of the continuum spectrum in millimeter/submillimeter wavelengths measured by ALMA. This decomposition is not unique but is tweaked to make the millimeter and submillimeter continuum dominated by the jet and the core, respectively.

KVN observations at 86 GHz have revealed that HCN and HCO^+ absorbing clumps are smaller than 0.1 pc and locate on the western receding jet 0.24–0.27 pc offset from the continuum peak implying complex kinematics in the vicinity of the AGN, such as inflow, outflow, and turbulence (Sawada-Satoh et al. 2016, 2019). The HCN absorption is dominated by two redshifted components at 149 and 212 km s^{-1} , which represent the redshifted component in the ALMA results. The blueshifted component with the peak opacity of 0.0035 measured by ALMA was not identified with KVN where the rms noise level was 0.035 in the normalized spectrum and the bandwidth of 128 MHz was not sufficient to determine a line-free baseline (Sawada-Satoh et al. 2016). The KVN HCO^+ absorption profile with an FWHM of $272 \pm 50 \text{ km s}^{-1}$ covers the systemic velocity (Sawada-Satoh et al. 2019), which is more consistent with the ALMA millimeter absorption. While the western receding jet casts both redshifted and blueshifted HCO^+ absorption, the eastern approaching jet does not show a clear absorption feature. A higher dynamic range VLBI observation is necessary to reproduce the ALMA results.

In view of the characteristics of the continuum components, millimeter and submillimeter absorbers are expected to locate where they mainly cover the jet and the core, respectively, as illustrated in Figure 7. This model predicts a longer line of sight toward the western receding side than that toward the eastern

approaching side to generate the asymmetric line profiles, with a greater optical depth in the redshifted component, as is observed in millimeter absorption. The model interprets the velocity width of the submillimeter absorption as the turbulent motion. In addition, the redshifted and blueshifted millimeter absorptions represent dragged gas flow by the approaching and receding jets, respectively.

An alternative explanation for the redshifted and blueshifted millimeter absorption is that clumps inside the torus are orbiting the core and pass across the line of sight to the continuum emission. In this case, the millimeter absorber is expected to locate at a further distance from the core than the submillimeter absorbers to explain the lower excitation temperature. Since the jets are well collimated and are expected to align with the orbital axis, a noncircular orbit is required to produce the redshifted and blueshifted absorption profiles.

3.4. Origin of Sulfur-bearing Molecules

In protoplanetary disks, sulfur-bearing molecules are known to trace the evaporation of icy components of dust. Nomura et al. (2020) calculated the evolution of fractional abundances of H_2S , SO, SO_2 , and CS under a given temperature and demonstrated that evaporated H_2S is destroyed by gas-phase reactions to form SO and SO_2 , and these will be frozen out on grains if the dust temperature is colder than 60 and 130 K, respectively.

The SO-to-CS abundance ratio in protostars is spread throughout various ranges: $N(\text{SO})/N(\text{CS}) < 0.11$ in the solar-analog IRAS 16293-2422 B (Drozdovskaya et al. 2018), 1.7–37.5 in 15 positions of molecular shocks in the low-mass protostar NGC 1333 IRAS 2 (Wakelam et al. 2005), 1.1–1.9 in the shocked region of class 0 protostar L1157 outflow (Bachiller & Perez Gutierrez 1997), and $3_{-2}^{+13} \times 10^2$ in the Class I protostellar source Elias 29 (Oya et al. 2019). The ratio in NGC 1052 is 6.1 ± 0.28 and 2.55 ± 0.05 for millimeter and submillimeter¹⁷ absorption, respectively, which are within the

¹⁷ Submillimeter column densities are derived using EW values of the SO 5_5-4_4 , 8_7-7_6 , 8_8-7_7 , and 8_9-7_8 transitions and CS $7-6$, HCN $4-3$, $\text{HCO}^+ 4-3$ in Kameno et al. (2020) and applying $T_{\text{ex}} = 344 \text{ K}$.

NGC 1052 Continuum Spectrum

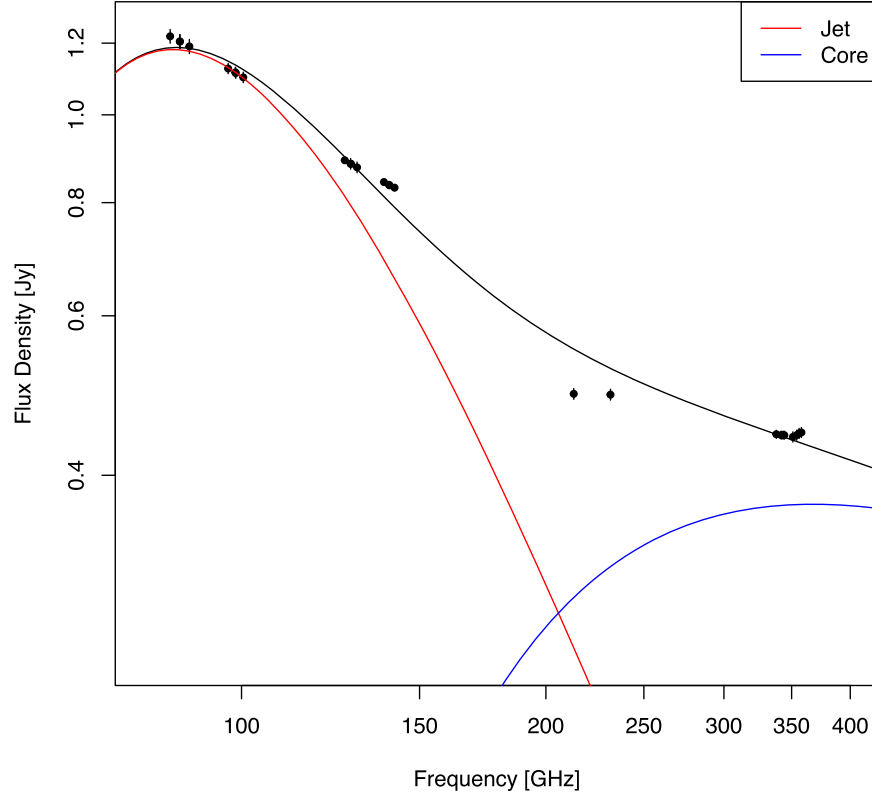


Figure 6. A possible decomposition of the continuum spectrum of NGC 1052 in millimeter/submillimeter wavelengths. The black dots represent ALMA measurements in this paper and those in Kameno et al. (2020). Jet (red) and core (blue) components are indicated by free-free absorbed synchrotron spectra with the spectral indices of -3 and -0.5 , respectively. Note that the decomposition is not unique but is tweaked to make the continuum in the millimeter and submillimeter wavelengths dominated by the jets and the core, respectively.

range of protostars and match the molecular shocks in NGC 1333 IRAS 2.

The ratios of SO-to-HCN and SO-to-HCO⁺ integrated line intensities in nearby galaxies are summarized in Table 4. NGC 1052 shows significantly higher SO-to-HCN and SO-to-HCO⁺ ratios than other galaxies. SO (8₈–7₇):HCO⁺ (4–3) = 1:26 and 1:3 in the ultraluminous infrared galaxy, IRAS 20551-4250 and NGC 1052. SO (3₂–2₁):HCN (1–0):HCO⁺ (1–0) = 1:33:17, 1:17:14, 1:13:9, and 1:2:0.8 in the Seyfert galaxy NGC 1068, in the starburst galaxies NGC 253 and IC 342, and NGC 1052, respectively.

The SO-to-HCO⁺ abundance ratio in NGC 1052 submillimeter absorption is derived to 4.63 ± 0.03 applying $T_{\text{ex}} = 344$ K. This value is probably overestimated because HCO⁺ is optically thick as implied by the high H¹³CN-to-H¹²CN ratio (Kameno et al. 2020). The ratio will be 0.95 ± 0.03 after applying correction with the ¹²C-to-¹³C abundance ratio of ~ 50 and the covering factor of $f_{\text{cov}} = 0.17$. That is significantly higher than the SO-to-HCO⁺ abundance ratio of 0.35 ± 0.23 in IRAS 20551-4250, applying $T_{\text{ex}} = 36$ K (Imanishi et al. 2017).

The SO-to-HCN abundance ratio in millimeter absorption is derived to 0.78 ± 0.03 , with $T_{\text{ex}} = 26$ K. This value will be corrected to 0.07 ± 0.02 by the ¹²C-to-¹³C abundance ratio and the covering factor. Although the excitation temperatures in NGC 1068, NGC 253, and IC 342 are unknown, $T_{\text{ex}} = 20$ –500 K yields the SO-to-HCN abundance ratio of 0.04–0.06, 0.08–0.11, and 0.11–0.14, respectively (Takano et al. 2019).

Thus, the opacity-corrected SO-to-HCN abundance ratio of millimeter absorption in NGC 1052 is comparable to that in other nearby galaxies.

The torus in NGC 1052 is considered to be dust-rich as a reservoir of sulfur-bearing molecules. Barth et al. (1999) revealed polarized broad H α emission, indicating the presence of dust torus, which obscures direct light from the broad line region (BLR). The BLR light only escapes in the polar-axis direction and scattered light can be observed. Thus, it is natural to consider the presence of dust grains in the molecular torus. A high SO-to-HCO⁺ abundance ratio in submillimeter absorption is interpreted by the evaporation of sulfur-bearing molecules from dust grains under high temperatures > 130 K.

The millimeter absorber is cooler than the freeze-out temperature, and contains redshifted and blueshifted velocity components up to 166 km s^{-1} with a narrow width of $< 65 \text{ km s}^{-1}$, and the SO-to-HCN abundance ratio is comparable to other nearby galaxies. A plausible interpretation for the redshifted and blueshifted millimeter absorber is that they are downstream of the submillimeter absorber dragged by the jets. Another possibility is that orbiting clumps pass across the line of sight toward the millimeter continuum source by chance. High-dynamic-range VLBI monitoring is needed to clarify the location and dynamics of the millimeter and submillimeter absorbers.

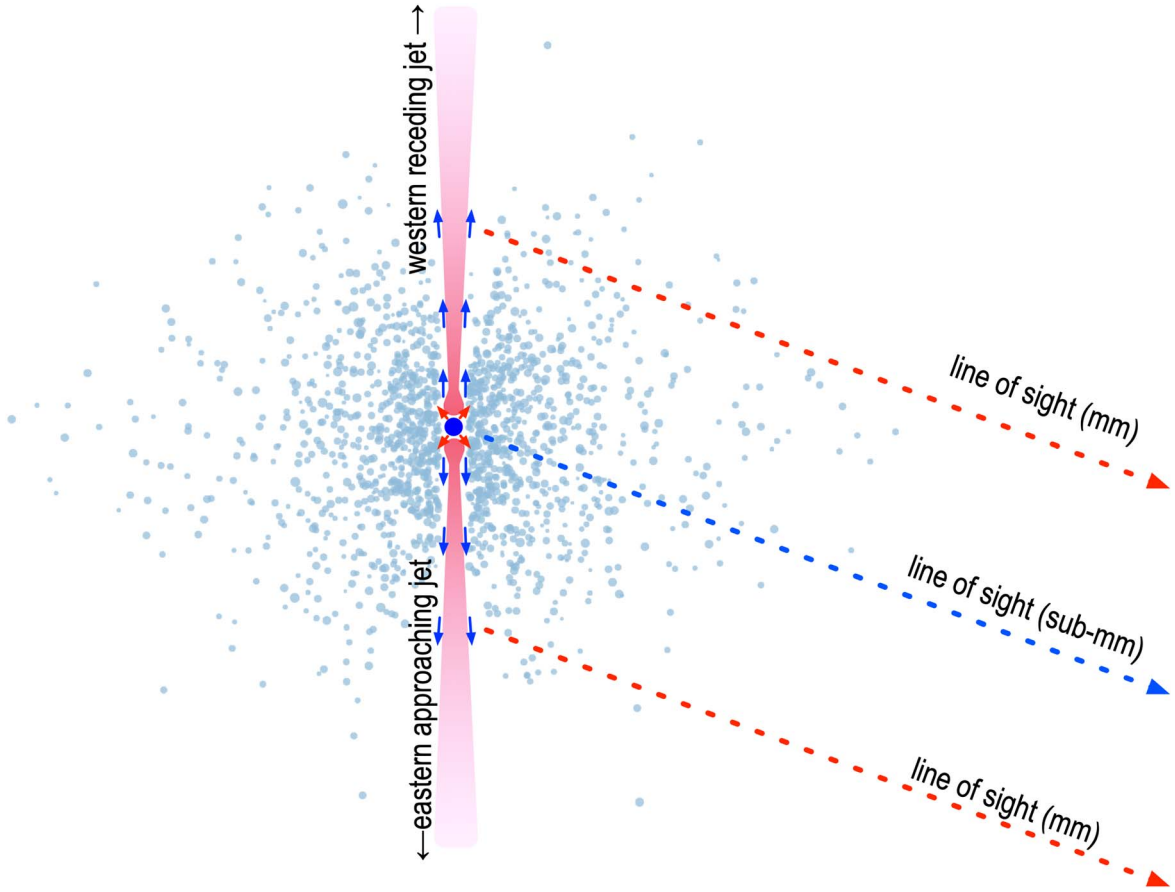


Figure 7. Schematic diagram of the torus composed of molecular/dusty clumps (pale blue). The core (blue circle) contains the central engine and the jet-launching region with submillimeter flat-spectrum synchrotron emission. The core is hidden in the low-frequency regime due to free-free absorption in the inner area of the torus. High-pressure outflows (red arrows) from the core interact with the inner wall of the torus. HCN, HCO^+ , and sulfur-bearing molecular gas evaporate from dust grains in the torus by the shock and produce submillimeter absorption features. The reverse shock collimates the jet along the polar axis. The jet emits optically thin synchrotron radiation off the torus. The jet drags molecular gas downstream (blue arrows), which produce millimeter absorption features. The line of sight toward the western receding side has greater optical depth than the eastern approaching side to generate the asymmetric line profiles.

3.5. The Heat Source

Dust grains with a radius of r emit a blackbody radiation of

$$P_{\text{rad,out}} = 4\pi r^2 \sigma_s T^4, \quad (2)$$

where σ_s is the Stefan–Boltzmann constant. If we apply $T = 344$ K and $r = R = 2.4$ pc (see Section 3.2), the radiation power of the whole torus will be $P_{\text{rad,out}} = 5.5 \times 10^{37}$ W, which exceeds the bolometric luminosity by two orders of magnitude. Therefore, the high temperature must appear only in a small fraction of the torus body. The radiation quickly cools the gas in the torus unless a heat source is present. In this section, we attempt to examine possible heating mechanisms to maintain such a high temperature of gas and dust in the torus.

3.5.1. Jet–Torus Interaction

NGC 1052 emanates sub-relativistic double-sided jets with a bulk speed of $0.26c$ – $0.53c$ (Vermeulen et al. 2003). The width of the jets is strongly confined to 0.016 pc ($1.3 \times 10^3 R_g$) inside $10^4 R_g$ from the nucleus (Nakahara et al. 2020; Baczko et al. 2022), implying a pressure gradient of the torus. Interaction between the relativistic jets and the confining molecular torus can cause shock that heats gas and dust.

The kinetic power of the jets is estimated as

$$P_{\text{jet,tot}} = \frac{1}{2} \pi r_j^2 \rho_j v_j^3, \quad (3)$$

where $r_j = 0.008$ pc is the radius of the cylindrical jets, ρ_j is the density, and $v_j = 0.26c$ is the jet speed. At the shock front between the torus gas and jets with the overpressure factor of ~ 1.5 (Fromm et al. 2019), we have

$$\rho_j v_j^2 = 1.5 \rho_t v_s^2, \quad (4)$$

where v_s is the advancing speed of the shock. The mean torus gas density, ρ_t , has been estimated as $n_{\text{H}_2} = 4.4 \times 10^6 \text{ cm}^{-3}$ (Kameno et al. 2020). Taking $v_s \simeq \Delta V_{\text{wing}} = 350 \text{ km s}^{-1}$ and $v_j = 0.26c$, we have $\rho_j = 4.4 \times 10^{-19} \text{ kg m}^{-3}$ and $P_{\text{jet,tot}} = 2.0 \times 10^{34} \text{ W}$, which corresponds to 10% of the bolometric luminosity of the AGN.

For the radiative cooling (Equation (2)) localized in the shock-heating region of r_j , we have $P_{\text{rad,out}} = 6 \times 10^{32} \text{ W}$ or 3% of the kinetic power of the jets. Therefore, the jet–torus interaction can account for the heating of gas and dust with a fractional amount of jet power. Because this model presumes localized heating within collimated jet width, it requires less energy injection than heating the whole torus.

Table 4
Integrated Line Intensity

Galaxy	HCO ⁺ (4–3) Jy km s ^{−1}	SO (8 ₈ –7 ₇) Jy km s ^{−1}	HCN (1–0) Jy km s ^{−1}	HCO ⁺ (1–0) Jy km s ^{−1}	SO (3 ₂ –2 ₁) Jy km s ^{−1}	References
(1)	(2)	(3)	(4)	(5)	(6)	(7)
IRAS 20551-4250	16.9 ± 0.2	0.64 ± 0.15				1
NGC 1068			26.4 ± 0.6	13.3 ± 0.7	0.8 ± 0.2	2
NGC 253			70 ± 1	59 ± 1	4.2 ± 0.3	2
IC 342			11.6 ± 0.1	8.4 ± 0.1	0.9 ± 0.1	2
NGC 1052 (EW: km s ^{−1})	15.9 ± 0.4	7.9 ± 0.5	4.95 ± 0.07	1.83 ± 0.13	2.33 ± 0.11	3, 4

Note. References: 1. Imanishi et al. (2017), 2. Takano et al. (2019), 3. Kameno et al. (2020), 4. This work.

Another advantage of this model is to naturally explain the evaporation of sulfur-bearing molecules from the dust mantle via shocks generated by a jet–torus interaction, and the presence of cool downstream gas to show millimeter absorption features. Future millimeter/submillimeter VLBI spectral images would unveil the temperature distribution of sulfur-bearing molecules along the jets to clarify the cooling mechanism.

In the following subsections, we consider other mechanisms for heating the gas in which the SO feature resides.

3.5.2. AGN Radiation

Here we examine whether the bolometric luminosity of $L_{\text{bol}} = 2 \times 10^{35} \text{ W}$ is enough to maintain the warm environment in the torus. A dust grain with a radius of r at the distance $R = 2.4 \text{ pc}$ from the nucleus receives a radiation power of $P_{\text{rad,in}} = L_{\text{bol}} \frac{r^2}{4R^2}$. Under the balance $P_{\text{rad,in}} = P_{\text{rad,out}}$, we have $L_{\text{bol}} = 16\pi R^2 \sigma_s T^4$ and then $T = 60 \text{ K}$. This indicates that AGN radiation cannot account for heating the gas and dust in the 2.4 pc torus. Radiative heating to 344 K would be realized closer to the nucleus by a factor of 33, i.e., $R \sim 0.07 \text{ pc}$.

3.5.3. Accretion

Accretion matter converts its potential energy into kinetic energy by 50% and dissipates by 50%. Here we examine whether dissipation can account for the heating of gas and dust heating.

Under the gravity of $F_G = \frac{GM_{\text{BH}}}{R^2}$, the dissipation rate for a unit mass is $\frac{1}{2}F_G v_{\text{acc}}$, where v_{acc} is the accretion velocity that must be less than the absorption-line velocity width $\Delta V_{\text{wing}} = 350 \text{ km s}^{-1}$. For a dust grain with a mass of $m_{\text{dust}} = \frac{4\pi}{3}\rho r^3$, the dissipation power is estimated as

$$P_{\text{acc,in}} = \frac{2\pi}{3} \frac{GM_{\text{BH}}}{R^2} \rho r^3 v_{\text{acc}}. \quad (5)$$

Comparing Equation (5) with the radiative cooling (Equation (2)) for the dust grain, we have

$$\frac{P_{\text{acc,in}}}{P_{\text{rad,dust}}} = \frac{GM_{\text{BH}} \rho r v_{\text{acc}}}{6\sigma_s R^2 T^4} = 3 \times 10^{-7} \left(\frac{M_{\text{BH}}}{1.5 \times 10^8 M_{\odot}} \right) \times \left(\frac{\rho}{10^3 \text{ kg m}^{-3}} \right) \left(\frac{R}{2.4 \text{ pc}} \right)^{-2} \left(\frac{T}{344 \text{ K}} \right)^{-4} \left(\frac{r}{1 \mu\text{m}} \right).$$

Thus, accretion power would be a significant heating process at a much inner region of $\sim 0.001 \text{ pc}$ but cannot account for the gas and dust heating at $R = 2.4 \text{ pc}$.

3.5.4. Star Formation

Starburst activity in a circumnuclear disk or a molecular torus could be the origin of the heat source in some Seyfert galaxies. Starburst characteristics in the disk or clumpy torus can be determined by Toomre's Q parameter defined as $Q = \frac{\sigma_R \kappa}{\pi G \Sigma}$, where σ_R is the velocity width, κ is the epicyclic frequency, and Σ is the surface density (Vollmer et al. 2008; Izumi et al. 2016).

As shown in Kameno et al. (2020), the circumnuclear disk in NGC 1052 is too gas-poor to drive mass accretion via ongoing star formation. For the molecular torus, we estimate $Q \sim 8$, applying $\Sigma = \frac{M_{\text{H}_2}}{\pi R^2} = 7.2 \times 10^5 M_{\odot} \text{ pc}^{-2}$, the velocity width of $\sigma_R = 350 \text{ km s}^{-1}$, and $\kappa = V_{\text{rot}}/R = 8.1 \times 10^{12} \text{ rad s}^{-1}$. Thus, it is classified as a massive, opaque, collisional disk according to Vollmer et al. (2008) where a star formation rate does not play a significant role compared with cloud collisions.

4. Conclusions

We have probed the absorption features of sulfur-bearing molecules, H₂S, SO, SO₂, and CS, toward millimeter and submillimeter continuum emission in the radio galaxy NGC 1052, and obtained clues on the physical properties of the molecular torus as summarized below.

1. The EWs of SO absorption are comparable to those of HCN and HCO⁺. After correcting for optical depth and covering factor, submillimeter absorption shows a significantly higher SO-to-HCO⁺ abundance ratio than the ultraluminous infrared galaxy, IRAS 20551-4250 does. The SO-to-HCN abundance ratio in millimeter absorption is comparable to that in nearby starburst and Seyfert galaxies. The SO-to-CS abundance ratio matches molecular shocks in the low-mass protostar NGC 1333 IRAS 2.
2. While submillimeter HCN and SO absorption profiles are simple single components centered at the systemic velocity, millimeter absorption is a multicomponent asymmetric profile with a peak and sharp edge in a redward and a shallower blueward slope. The difference in the profiles is ascribed to the location of the background continuum, the core, and the jets in submillimeter and millimeter regimes, respectively.
3. The submillimeter SO absorption indicates the rotation temperature of $T_{\text{rot}} = 344 \pm 43 \text{ K}$. That is greater than the freeze-out temperatures of SO₂ and SO, and is consistent with the presence of 22 GHz H₂O masers and vibrationally excited HCN and HCO⁺ absorption lines in the molecular torus.

4. Jet–torus interaction is the most plausible heat source for the gas and dust in the torus. Our results support that the torus is working for jet collimation inside $10^4 R_s$.
5. The millimeter SO absorption features’ fit of 26 ± 4 K, is significantly cooler than that of the submillimeter SO absorption features. The millimeter continuum is dominated by jets and the cooler SO gas is considered to be dragged downstream flows. The asymmetric millimeter absorption profiles can be generated by different lines of sight through the absorbers toward the western receding side and eastern approaching side.







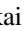

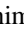

Following the millimeter/submillimeter absorption study with ALMA detecting a jet–torus interaction, we want to acquire a spatially resolved distribution of the temperature and velocity field of the absorber using millimeter/submillimeter spectral VLBI observations.

We thank the anonymous reviewer for their thorough and constructive suggestions. This paper makes use of the following ALMA data: ADS/JAO.ALMA#2013.1.01225.S and ADS/JAO.ALMA#2016.1.00375.S. ALMA is a partnership of ESO (representing its member states), NSF (USA), and NINS (Japan), together with NRC (Canada), MOST and ASIAA (Taiwan), and KASI (Republic of Korea), in cooperation with the Republic of Chile. The Joint ALMA Observatory is operated by ESO, AUI/NRAO, and NAOJ. This work is supported by JSPS KAKENHI 18K03712 and 21H01137. N.K. is supported by JSPS KAKENHI 19K03918. K.K. acknowledges the support of JSPS KAKENHI grant No. 17H06130. D. E. acknowledges support from (1) a Beatriz Galindo senior fellowship (BG20/00224) from the Spanish Ministry of Science and Innovation, (2) projects PID2020-114414GB-I00 and PID2020-113689GB-I00 financed by MCIN/AEI/10.13039/501100011033, (3) project P20_00334 financed by the Junta de Andalucía, and (4) project A-FQM-510-UGR20 of the FEDER/Junta de Andalucía-Consejería de Transformación Económica, Industria, Conocimiento y Universidades.

Facility: ALMA.

Software: CASA 6.4.0.16.

ORCID iDs

Seiji Kameno  <https://orcid.org/0000-0002-5158-0063>
 Satoko Sawada-Satoh  <https://orcid.org/0000-0001-7719-274X>
 C. M. Violette Impellizzeri  <https://orcid.org/0000-0002-3443-2472>
 Kotaro Kohno  <https://orcid.org/0000-0002-4052-2394>
 Sergio Martín  <https://orcid.org/0000-0001-9281-2919>
 Daniel Espada  <https://orcid.org/0000-0002-8726-7685>
 Naomasa Nakai  <https://orcid.org/0000-0002-5461-6359>
 Hajime Sugai  <https://orcid.org/0000-0001-6501-3871>
 Yuichi Terashima  <https://orcid.org/0000-0003-1780-5481>
 Minju M. Lee  <https://orcid.org/0000-0002-2419-3068>

Nozomu Kawakatu  <https://orcid.org/0000-0003-2535-5513>

References

- Adande, G. R., Edwards, J. L., & Ziurys, L. M. 2013, *ApJ*, **778**, 22
 Antonucci, R. 1993, *ARA&A*, **31**, 473
 Bachiller, R., & Pérez Gutiérrez, M. 1997, *ApJL*, **487**, L93
 Baczko, A. K., Ros, E., Kadler, M., et al. 2022, *A&A*, **658**, A119
 Baczko, A. K., Schulz, R., Kadler, M., et al. 2016, *A&A*, **593**, A47
 Baczko, A. K., Schulz, R., Kadler, M., et al. 2019, *A&A*, **623**, A27
 Baloković, M., Cabral, S. E., Brenneman, L., & Urry, C. M. 2021, *ApJ*, **916**, 90
 Barth, A. J., Filippenko, A. V., & Moran, E. C. 1999, *ApJL*, **515**, L61
 Braatz, J. A., Wilson, A. S., & Henkel, C. 1994, *ApJL*, **437**, L99
 Braatz, J. A., Wilson, A. S., Henkel, C., Gough, R., & Sinclair, M. 2003, *ApJS*, **146**, 249
 Claussen, M. J., Diamond, P. J., Braatz, J. A., Wilson, A. S., & Henkel, C. 1998, *ApJL*, **500**, L129
 Drozdovskaya, M. N., van Dishoeck, E. F., Jørgensen, J. K., et al. 2018, *MNRAS*, **476**, 4949
 Elitzur, M., Hollenbach, D. J., & McKee, C. F. 1989, *ApJ*, **346**, 983
 Fromm, C. M., Younsi, Z., Baczko, A., et al. 2019, *A&A*, **629**, A4
 Gallimore, J. F., Elitzur, M., Maiolino, R., et al. 2016, *ApJL*, **829**, L7
 García-Burillo, S., Combes, F., Almeida, C. R., et al. 2016, *ApJL*, **823**, L12
 Guo, Q., Zhang, J. S., & Wang, J. 2014, *JApA*, **35**, 223
 Imanishi, M., Nakanishi, K., & Izumi, T. 2017, *ApJ*, **849**, 29
 Impellizzeri, C. M. V., Gallimore, J. F., Baum, S. A., et al. 2019, *ApJL*, **884**, L28
 Impellizzeri, V., Roy, A. L., & Henkel, C. 2008, *PoS*, **072**, 033
 Izumi, T., Kawakatu, N., & Kohno, K. 2016, *ApJ*, **827**, 81
 Kadler, M., Ros, E., Lobanov, A. P., Falcke, H., & Zensus, J. A. 2004, *A&A*, **426**, 481
 Kameno, S., Inoue, M., Wajima, K., Sawada-Satoh, S., & Shen, Z.-Q. 2003, *PASA*, **20**, 134
 Kameno, S., Nakai, N., Sawada-Satoh, S., Sato, N., & Haba, A. 2005, *ApJ*, **620**, L15
 Kameno, S., Sawada-Satoh, S., Impellizzeri, C. M. V., et al. 2020, *ApJ*, **895**, 73
 Kameno, S., Sawada-Satoh, S., Inoue, M., Shen, Z.-Q., & Wajima, K. 2001, *PASJ*, **53**, 169
 Kellermann, K. I., Vermeulen, R. C., Cohen, M. H., & Zensus, J. A. 1999, *AAS Meeting Abstracts*, **194**, 20.02
 Lahuis, F., Spoon, H. W. W., Tielens, A. G. G. M., et al. 2007, *ApJ*, **659**, 296
 Liszt, H., & Lucas, R. 2004, *A&A*, **428**, 445
 Martín, S., Martín-Pintado, J., Mauersberger, R., Henkel, C., & García-Burillo, S. 2005, *ApJ*, **620**, 210
 Martín, S., Mauersberger, R., Martín-Pintado, J., García-Burillo, S., & Henkel, C. 2003, *A&A*, **411**, L465
 Minh, Y. C., Muller, S., Liu, S. Y., & Yoon, T. S. 2007, *ApJL*, **661**, L135
 Nakahara, S., Doi, A., Murata, Y., et al. 2020, *AJ*, **159**, 14
 Nomura, H., Higuchi, A., Sakai, N., et al. 2020, in *IAU Symp. 345, Origins: From the Protosun to the First Steps of Life*, ed. B. G. Elmegreen, L. V. Tóth, & M. Güdel (Cambridge: Cambridge Univ. Press), 360
 Omar, A., Anantharamaiah, K. R., Rupen, M., & Rigby, J. 2002, *A&A*, **381**, L29
 Oya, Y., López-Sepulcre, A., Sakai, N., et al. 2019, *ApJ*, **881**, 112
 Pineau des Forets, G., Roueff, E., Schilke, P., & Flower, D. R. 1993, *MNRAS*, **262**, 915
 Sato, M. T., Aalto, S., Kohno, K., et al. 2022, *A&A*, **660**, A82
 Sawada-Satoh, S., Byun, D.-Y., Lee, S.-S., et al. 2019, *ApJL*, **872**, L21
 Sawada-Satoh, S., Kameno, S., Nakamura, K., et al. 2008, *ApJ*, **680**, 191
 Sawada-Satoh, S., Roh, D.-G., Oh, S.-J., et al. 2016, *ApJL*, **830**, L3
 Takano, S., Nakajima, T., & Kohno, K. 2019, *PASJ*, **71**, S20
 Vermeulen, R. C., Ros, E., Kellermann, K. I., et al. 2003, *A&A*, **401**, 113
 Vollmer, B., Beckert, T., & Davies, R. I. 2008, *A&A*, **491**, 441
 Wakelam, V., Ceccarelli, C., Castets, A., et al. 2005, *A&A*, **437**, 149
 Woo, J.-H., & Urry, C. M. 2002, *ApJ*, **579**, 530